Institute of Technology and Engineering (ITE)

Impact of Geometry Transfer Errors on Structural-ThermalOptical-Performance (STOP) Analysis in Spaceborne Optical Systems

Giorgi Kakabadze, Forschungszentrum Jülich,
Institute of Technology and Engineering (ITE)

Marian Partzsch, Forschungszentrum Jülich,
Institute of Technology and Engineering (ITE)

Jörg Wolters, Forschungszentrum Jülich,
Institute of Technology and Engineering (ITE)

Ghaleb Natour, Forschungszentrum Jülich,
Institute of Technology and Engineering (ITE)

Jül-4451

Mitglied der Helmholtz-Gemeinschaft

JÜLICH
Forschungszentrum

Berichte des Forschungszentrums Jülich
Jül-4451 · ISSN 0944-2952
Institute of Technology and Engineering (ITE)

Vollständig frei verfügbar über das Publikations-
portal des Forschungszentrums Jülich (JuSER)
unter www.fz-juelich.de/zb/openaccess

Forschungszentrum Jülich GmbH · 52425 Jülich
Zentralbibliothek, Verlag
Tel.: 02461 61-5220 · Fax: 02461 61-6103
zb-publikation@fz-juelich.de
www.fz-juelich.de/zb

This is an Open Access publication distributed under the terms of the **Creative Commons Attribution License 4.0**, which permits unrestricted use, distribution, and reproduction in any medium, provided the original work is properly cited.

Institute of Technology and Engineering (ITE)

Impact of Geometry Transfer Errors on Structural-ThermalOptical-Performance (STOP) Analysis in Spaceborne Optical Systems

Giorgi Kakabadze, Forschungszentrum Jülich,
Institute of Technology and Engineering (ITE)

Marian Partzsch, Forschungszentrum Jülich,
Institute of Technology and Engineering (ITE)

Jörg Wolters, Forschungszentrum Jülich,
Institute of Technology and Engineering (ITE)

Ghaleb Natour, Forschungszentrum Jülich,
Institute of Technology and Engineering (ITE)

Abstract

Thermal loading during on-orbit operations can induce significant structural deformations, which in turn can degrade the performance of optical devices used for scientific analyses. Accurate Structural-Thermal-Optical-Performance (STOP) analyses are therefore vital to predict image quality under coupled thermal and mechanical influences. An essential step in such multidisciplinary workflows of STOP analyses is the transfer of deformation data from thermo-mechanical simulations into optical analysis tools. This work highlights the challenges arising from the use of STL file formats for geometry transfer, where inaccuracies in topology representation introduce distortions that directly impact the fidelity of optical predictions. The implications of these artifacts on image quality are analysed and discussed within the framework of the SHIPAS project, a small satellite mission carrying a remote sensing payload for temperature field measurements in the upper atmosphere (60 km – 110 km). The study demonstrates how improper data transfer can undermine STOP analysis reliability and provides a newly developed algorithm, implemented as an ANSYS Parametric Design Language (APDL) script, that decomposes thermo-mechanically induced deformations of optical bodies into their individual components — rigid body translation, rotation, scaling, and asymmetric strain — and transfers them to the optical simulation environment without geometry format-induced distortions. As an illustration, the algorithm is applied to the optical subsystem of the satellite, demonstrating the elimination of file-format artifacts, thus, allowing the true influence of thermal deformations on image quality to be assessed reliably.

Acknowledgment:

This work was supported by Shota Rustaveli National Science Foundation of Georgia (SRNSFG) [grant number: JFZ-23-015] and the Institute of Technology and Engineering (ITE), Forschungszentrum Jülich.

Keywords: Structural-thermal-optical performance, satellite, optical ray tracing, polygonal.

Content

1 Introduction

During on-orbit missions objects face thermal loads, which can lead to significant thermal-based structural displacements. Such scenarios can lead to critical mission failures for various precise systems, like optical measuring instruments. To ensure good image quality of such systems, the influence of thermal deformations on the image quality has to be investigated and minimized (Yang, Yao, Cai, & Bi, 2021).

Structural-Thermal-Optical-Performance (STOP) analysis is the multidisciplinary approach to predict relevant image quality for optical systems undergoing significant thermal and mechanical loads. During such analysis it is crucial to define a certain workflow (Bolognese & Irish, 2015) and interfaces (Heijmans, Holzlöhner, & Müller, 2018) from one step to another.

The current work was performed under the SHIPAS project (Watt & Stricker, 2023), which is a remote sensing optical system on a small scale satellite, to perform temperature field measurements in high layers of the atmosphere, approximately from 60 km to 110 km altitude.

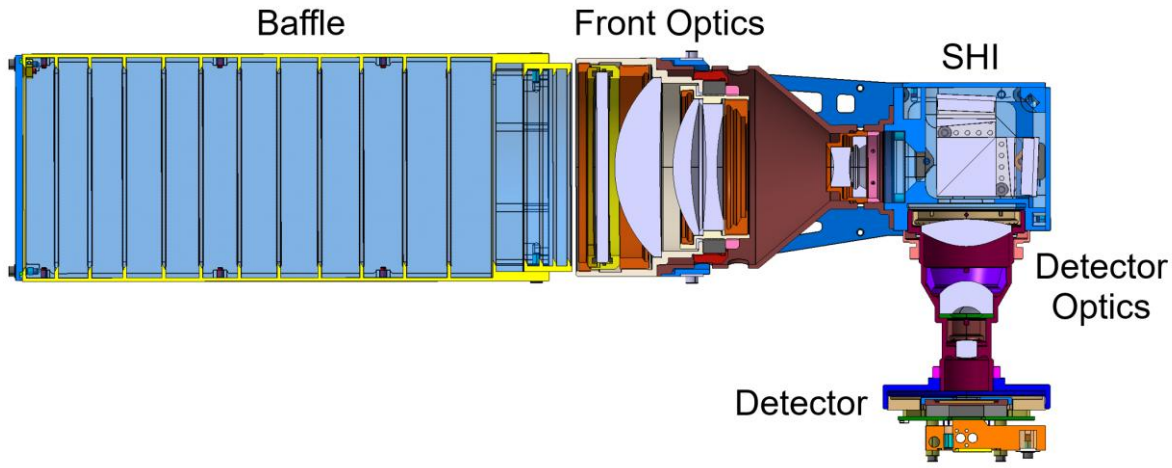

Figure 1. Cut view of SHIPAS schematics

The system consists of several subsystems (Figure 1):

- Baffle – constraints field of view and ensures blockage of straylight entrance into the system.
- Front optics – set of four lenses, which focuses incoming light into the spatial heterodyne interferometer.
- Spatial heterodyne interferometer (SHI) – assembly of beamsplitter and diffraction gratings, where optical interference is performed and light is redirected to the detector optics.
- Detector optics – set of three lenses, which brings light from the SHI to the detector.
- Detector – the last piece in the chain where the optical matrix is located and the final picture is retrieved.

For the test case, our main focus is the front optics subsystem, and as a control plane the first surface of SHI is taken (Figure 2).

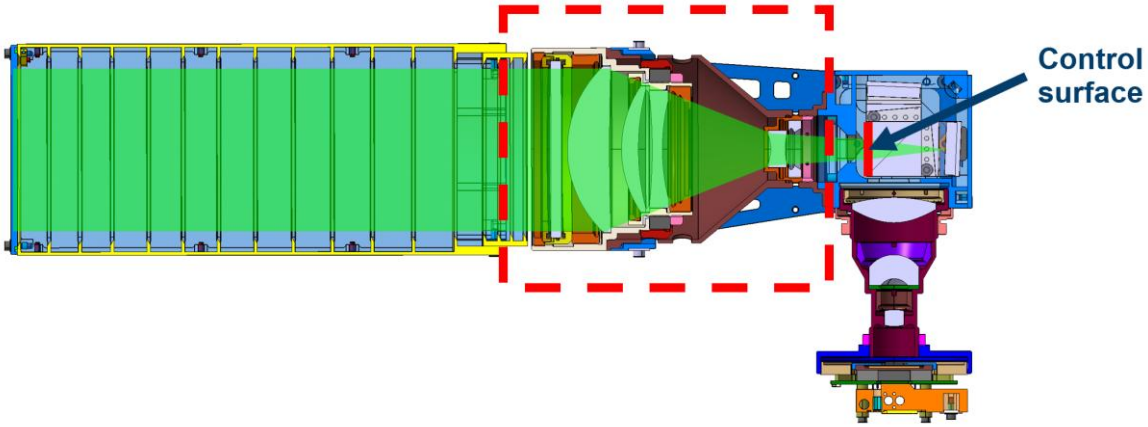

Figure 2. Isolated case of front optics and the control surface

2 STOP Workflow

Complex systems like satellites require interdisciplinary studies, especially while having optical systems on board. Extreme orbital environment affects the system in various ways, so simulations considering every aspect should be made. One of such multidisciplinary simulations is the STOP analysis and effective workflow is an essential part of this analysis.

Generally, a STOP analysis consists of 3 main stages:

1. Thermal: Determination of temperature fields that result from all relevant heat sources and thermal boundary conditions and which serve as thermal boundary condition for the structural stage.
2. Structural: Determination of deformed geometry (displacements) due to the temperature fields provided by step 1 and additional mechanical loads, if applicable.
3. Optical: Evaluation of the influence of the identified deformations on the image quality of the optical system.

If necessary, the system can be improved based on the findings obtained from the three stages.

Such kind of complex analysis requires various codes, or Multiphysics software packages that can simulate each step (Badás, et al., 2024). These software packages can be united in one environment or be independent ones.

In our case, the goal was to perform STOP analysis via Ansys Multiphysics software package. Here thermal and structural modules can be directly combined in the Workbench environment. However, Ansys Zemax 2024 R1 as an optical simulation software, is not part of this Workbench environment and stands as a separate module. This brings additional difficulties in a general workflow, while data from the structural stage cannot be transferred directly to the optical stage, like in the case with thermal and mechanical analysis (See Figure 3). An appropriate interface between the structural and optical stage is needed.

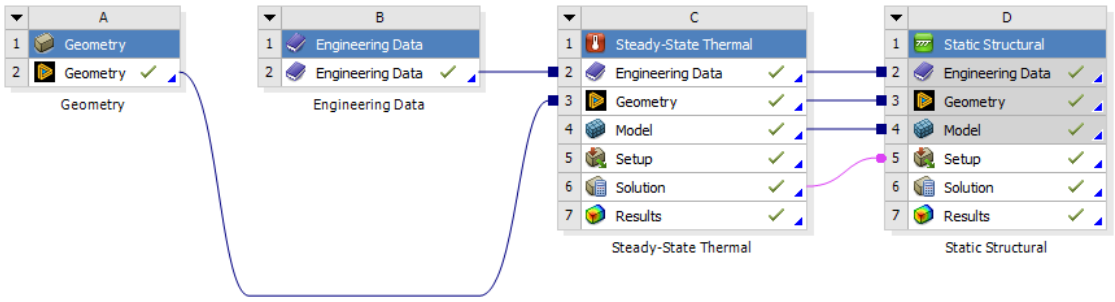

Figure 3. Data transition workflow in Ansys Workbench

Such workflow in Workbench ensures modular approach to the problem and provides established interfaces. This has a significant effect on the quality and time required for simulations in general.

3 Export methods from Workbench Mechanical

Since Zemax, which we use for optics simulations, is not part of the Workbench environment where thermo-mechanical simulations are performed, an interface to transfer the deformed geometry from the structural simulation to the optical simulation is needed.

By default, the only file format which can be exported from Ansys mechanical as a displaced structure geometry is STL file (Zhang, Chen, Cava, & Normanshire, 2025). Such format is accepted by Zemax optical ray tracing tool to be imported directly so that analysis can be performed. However, there is significant drawback in using STL file for precise simulations.

4 Nature of STL file

STL, which stands for Stereolithography, is a format of a 3D file used in various CAD software and mostly compatible with 3D printing technology. The main difference between normal CAD file and STL is that STL lacks internal volume of the body and consists of only external contours made via flat polygons instead of interpolated surfaces (shown in Figure 4) (Koppen, van der Kolk, Van Kempen, de Vreugd, & Langelaar, 2018). Such format ensures small size of a file, however, it only approximates the desired shape at some level.

In our case, the size of each polygonal surface is fully dependent on the mesh size and quality generated on the surface of our geometry. It means that increasing element number at the meshing phase can lead to better approximation of the surface of our part. On the other hand, significant increase in computational effort should be taken into account for all three phases of the STOP analyses. while still the negative effect of polygonal shaped surfaces during optical ray tracing will not be effectively eliminated.

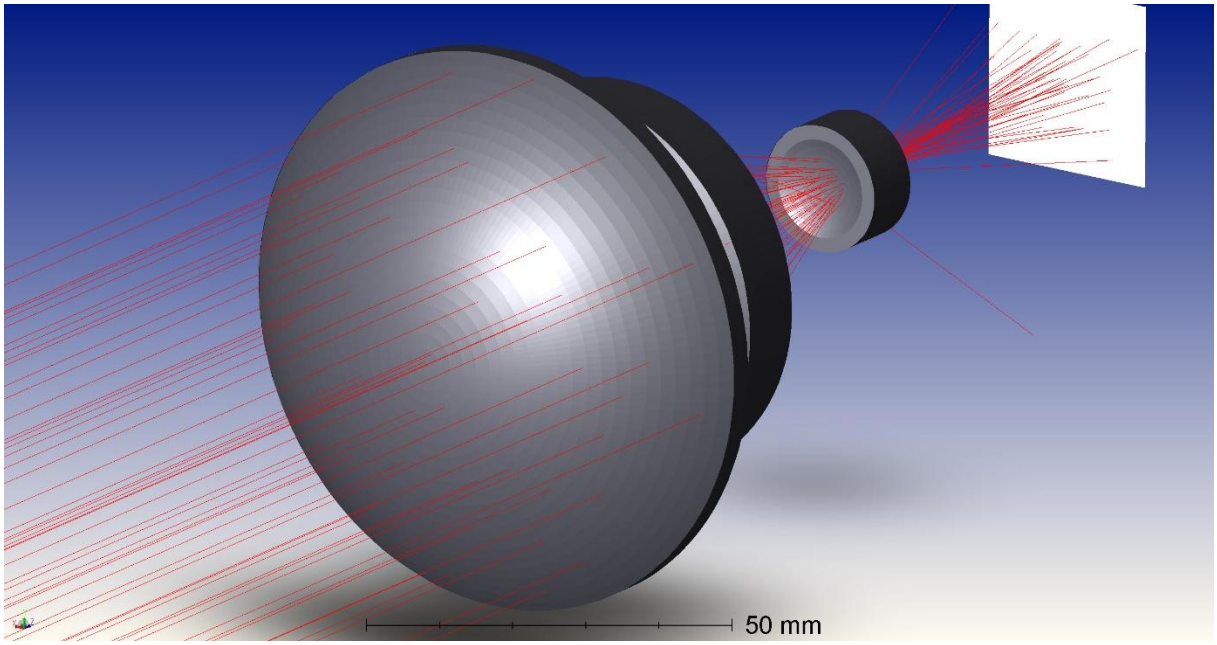

Figure 4. Lenses geometry in STL format imported in Ansys Zemax

5 Problems during optical ray tracing

As mentioned above, polygonal shapes on an external surface of the body cause significantly different optical characteristics compared to initially designed smooth shapes, simply because they redirect all rays in a different spatial direction (Haber, Draganov, & Krainak, 2022).

To substantiate this effect, exactly the same geometry of lenses from CAD software were saved in two different formats, STEP and STL, the first one providing ideal, smooth surface and the second providing discretized polygonal shape. After importing them in Zemax, two optical ray tracing simulations were made with identical scenarios, using circular light source and the significant difference was observed on a reference projection plane. Even without measuring any metrics, the effect of STL file was evident by visually comparing the pictures of irradiation.

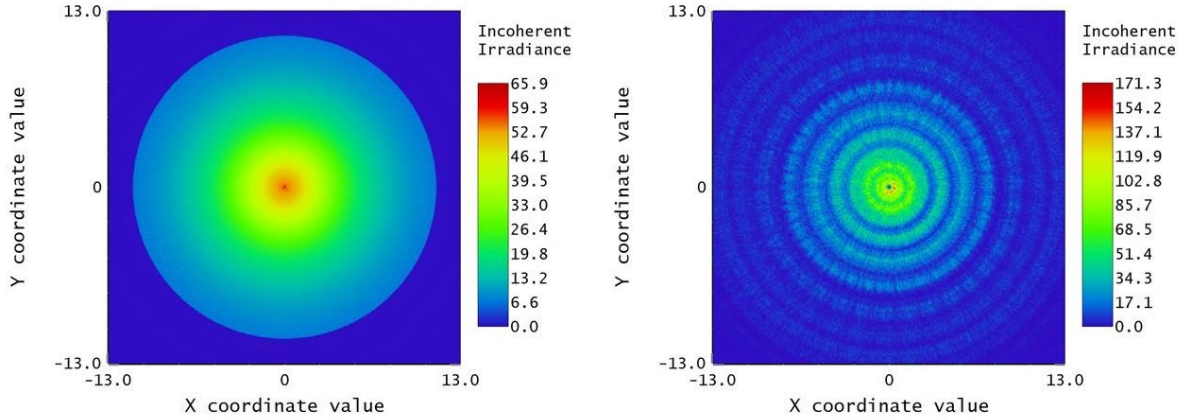

Figure 5. Comparison of ray tracing simulations results on STEP (left) and STL (right) files

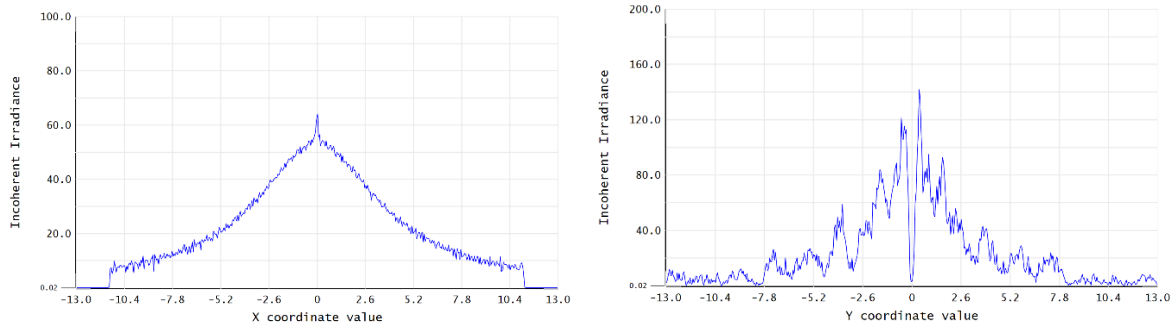

Figure 6. Cross section of ray distribution for STEP (left) and STL (right) files

As can be observed, simulation results using STEP file is much more like Gaussian distribution in shape, but mainly steady distribution, while STL file provides significant number of fluctuations and distorted steadiness, which are easily visible in the cross section of radiation intensity distribution presented on Figure 5 and Figure 6.

6 Topology problem solving

Except polygonal shape, the main issue with STL format is that it is not compatible with most industrial CAD software. Although it can be opened and visualized, it is usually not possible to further edit the geometry easily. Meanwhile, there is some software on the market (E.g. Free CAD, Rhino, etc.), which makes it possible to work with such format, edit it, manipulate it, etc.

One of the software packages is available in Ansys Workbench environment and it is called Space Claim, which is inbuilt CAD module and has a tool to smooth surfaces, which works for STL format as well. During analysis, that approach has been tested as well, however, the results were deficient (Figure 7). During editing process, some geometrical errors were revealed, like edge rounding or surface deformation, which lead to significantly different ray tracing picture compared to the original ideal case.

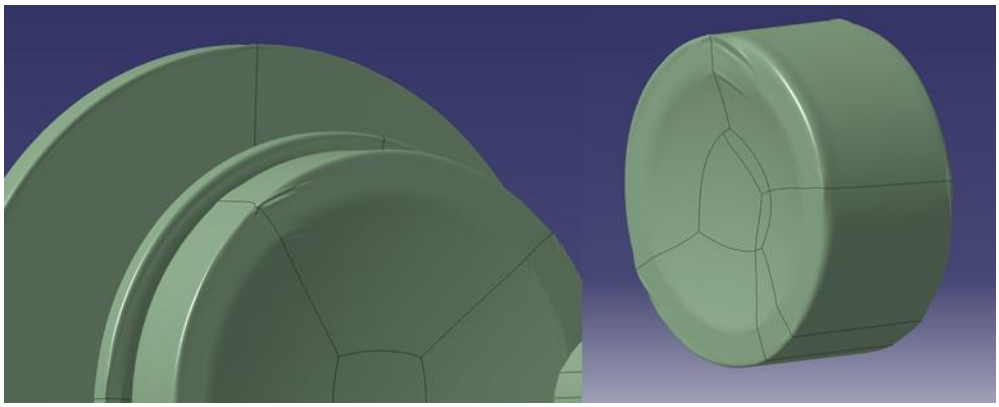

Figure 7. Geometrical errors after editing in Space Claim

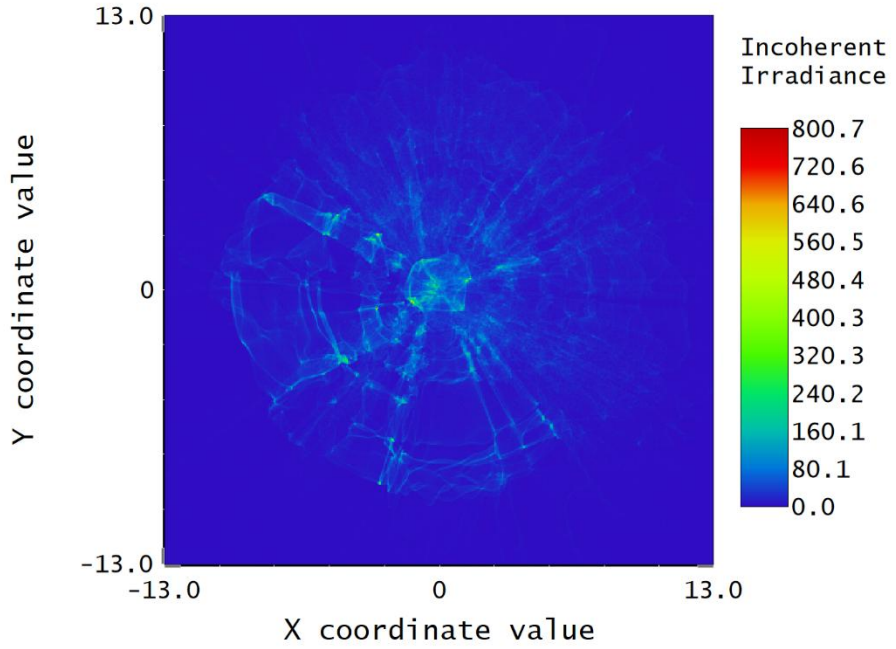

Figure 8. Ray tracing results with geometry edited in Space Claim

After redoing simulation wit STL geometry being smoothed in Space Claim, completely distorted result was obtained (Figure 8), while the actual image on the reference surface has lost all the contrast and ray distribution characteristics compare to the original STEP file.

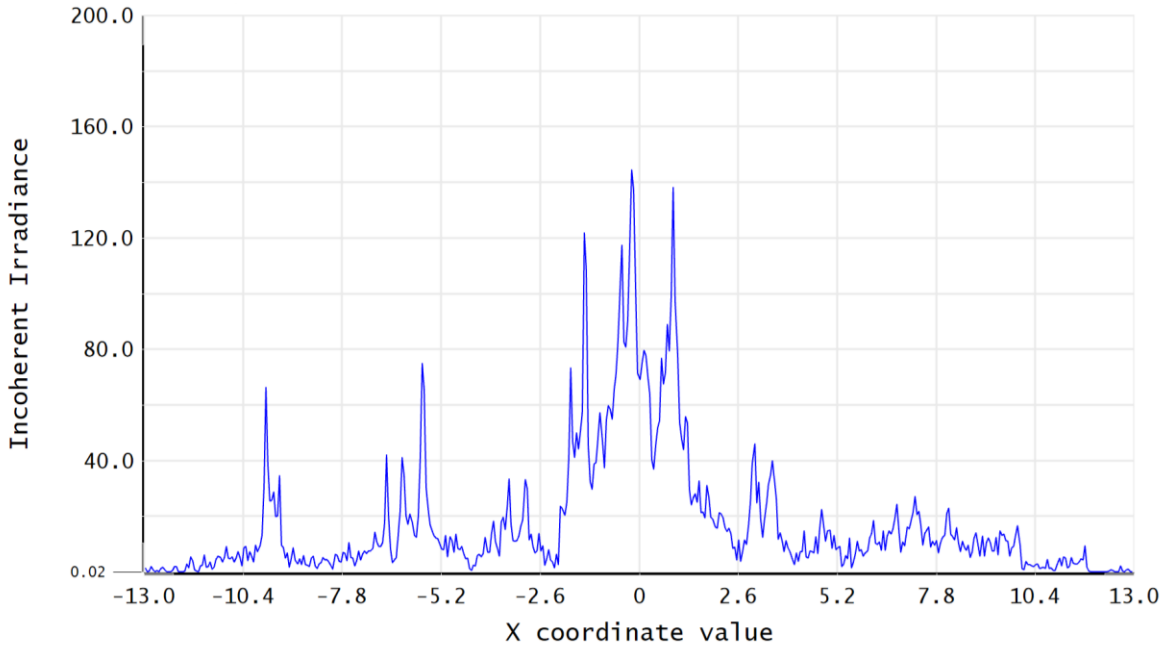

Figure 9. Cross section of ray distribution for file edited in Space Claim

Image distortion is also visible in a cross-section result of simulation (Figure 9) on smoothed file. It can be observed that after smoothing the polygonal surface of the STL geometry, the geometric characteristics of a lens are completely changed and distorted.

To avoid distortion of sharp edges of the lenses by smoothing in Space Claim (like shown in Figure 7), another approach for a single lens was tested. Here, smoothing was only performed for the front and rear surface of the lens separately and based on these two smoothed surfaces a new solid body was created in the CAD software CATIA V5 (Figure 10).

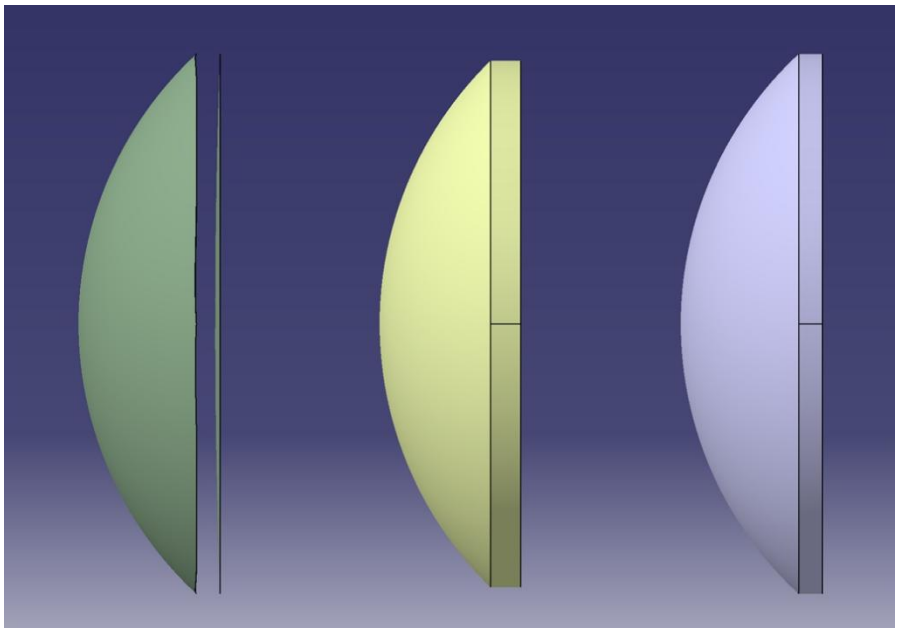

Figure 10. Solid body created from treated front and rear surfaces

However, even while body distortions at the edges have been eliminated, the optical ray tracing simulations did not provide predictable smooth contours, resulting in significantly distorted image quality, what can be seen in Figure 11 and Figure 12.

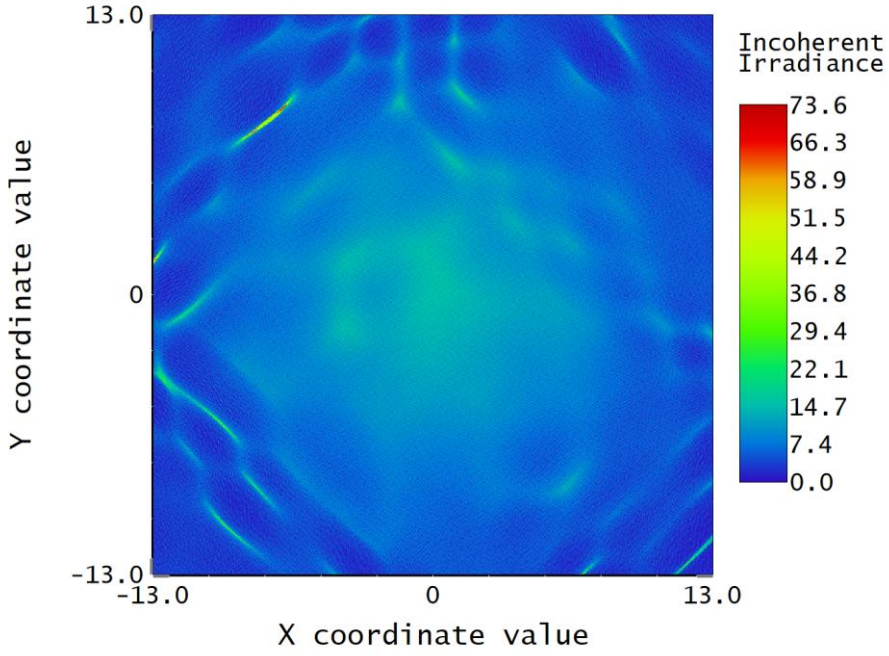

Figure 11. Detector view after analysis of surface treated lens

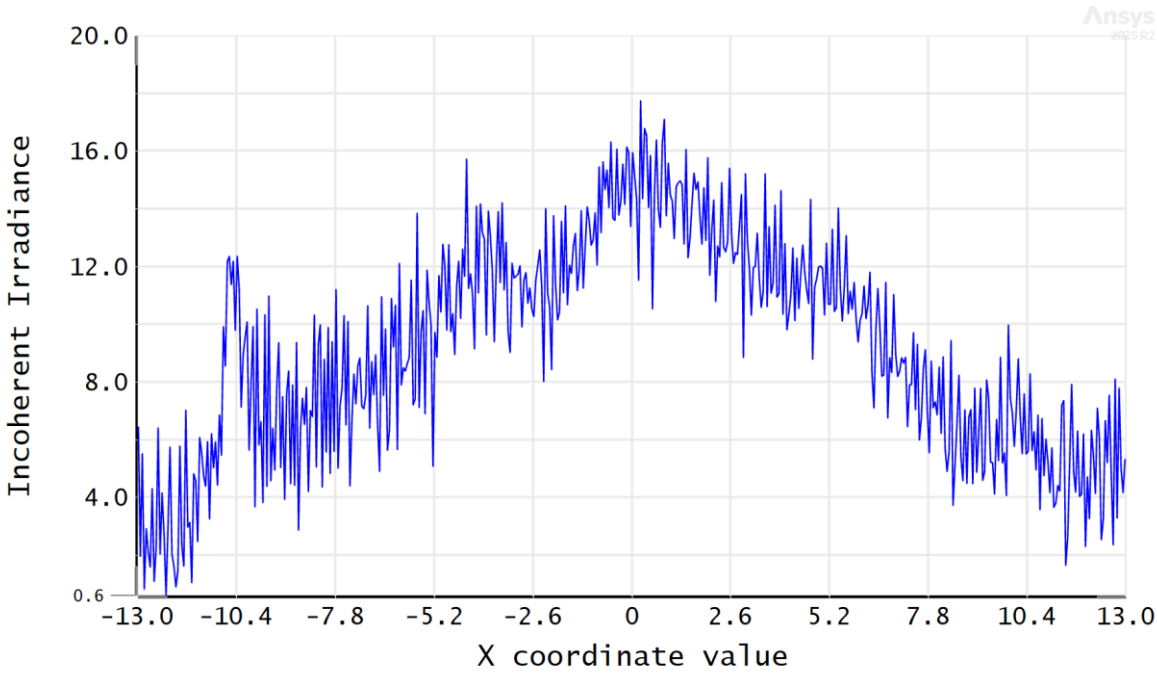

Figure 12. Cross-section view of surface treated lens results

Thus, after such manipulation on a geometry, following issues can still be observed:

- Geometrical error
- Increased computational resources
- Ray tracing error occurring
- bad image quality

Therefore, the smoothing approach via Space Claim is not feasible at all and a more efficient approach must be found to deal with the issue.

The most important aspect in the workflow is to somehow avoid using STL format at all. However, it is quite challenging, since Ansys only supports exporting deformed 3D geometry in that format.

One of the possibilities to approximate displaced structure in a more accurate way, is to use the element displacements originally calculated in the finite element simulation and recreate displaced geometry in a CAD software manually. In such approach, several aspects should be considered to create the new geometry of one lens in the optical system, such as axial displacements, rotations, shrinkage/scaling and asymmetric deformation. The last one is the most challenging part to reproduce in the CAD software, but due to the high rigidity of the lenses used in the optical system and the low mechanical stress on the individual lenses, asymmetric deformations will be very small and can therefore generally be neglected compared to the deformations in the overall structure of the optical system. To evaluate this, the level of such distortion will be compared to other contributors of deformation.

7 The algorithm of capturing displacements

After trying various approaches, an APDL (ANSYS Parametric Design Language) script was developed to determine the displacement, rotation, scaling and distortion of bodies with respect to their original centre of gravity. The gist of the algorithm is to isolate each of these contributions from the overall body displacements and provide separate values for the body of interest, so it

can be then remodelled to perform the optical ray tracing simulation afterwards. The APDL script is based on vector operations only (*V-commands) to speed up execution time significantly. The iterative algorithm is described in the following.

First, the local element coordinates $\vec{x}_i = \begin{pmatrix} x_i \\ y_i \\ z_i \end{pmatrix}$ relative to the centre of gravity are collected. Moreover, for each element the displacements $d\vec{x}_i = \begin{pmatrix} dx_i \\ dy_i \\ dz_i \end{pmatrix}$ are determined.

The mean body displacement $d\vec{x}_R$ is calculated by averaging the displacement values for all three axes. Since the mesh contains elements of varying sizes, a volume-weighted average was employed, leading to a more physically meaningful global measure. Afterwards, the remaining displacements $d\vec{x}_i'$, that result from rigid body rotation, expansion and distortion, were calculated.

$$d\vec{x}_R = \frac{\sum d\vec{x}_i \cdot V_i}{V_{tot}}; d\vec{x}_i' = d\vec{x}_i - d\vec{x}_R$$

The most crucial part of the algorithm is to describe 3D space rotation via a rotation vector and angle. Here the following approach was used. Considering the remaining element displacements $d\vec{x}_i'$ a resulting new element location is calculated:

$$\vec{x}'_i = \vec{x}_i + d\vec{x}_i'$$

For each coordinate axis, the original and new angular positions of the elements are determined by using the quadrant-aware inverse tangent function $\mathrm{atan2}(y, x)$. The rotational movement of the element around the corresponding axis is given by the difference between both angles. The mean value, weighted by the element volume V_i and – as an option - the distance to the axis of rotation ($R_{x,i} = \sqrt{y_i^2 + z_i^2}, R_{y,i} = \sqrt{x_i^2 + z_i^2}$ and $R_{z,i} = \sqrt{x_i^2 + y_i^2}$, respectively) is calculated for each coordinate axis, and this is used to determine an initial estimate for the global axis of rotation.

$$d\varphi_{x,i} = \varphi'_{x,i} - \varphi_{x,i} = atan2(y'_i; z'_i) - atan2(y_i; z_i)$$

$$d\varphi_{y,i} = \varphi'_{y,i} - \varphi_{y,i} = atan2(x'_i; -z'_i) - atan2(x_i; -z_i)$$

$$d\varphi_{z,i} = \varphi'_{z,i} - \varphi_{z,i} = atan2(x'_i; y'_i) - atan2(x_i; y_i)$$

$$d\varphi_{x,R} = \frac{\sum d\varphi_{x,i} \cdot V_i}{V_{tot}};\ d\varphi_{y,R} = \frac{\sum d\varphi_{y,i} \cdot V_i}{V_{tot}};\ d\varphi_{z,R} = \frac{\sum d\varphi_{z,i} \cdot V_i}{V_{tot}}$$

or

$$d\varphi_{x,R} = \frac{\sum d\varphi_{x,i} \cdot V_i \cdot R_{x,i}}{\sum V_i \cdot R_{x,i}};\ d\varphi_{y,R} = \frac{\sum d\varphi_{y,i} \cdot V_i \cdot R_{y,i}}{\sum V_i \cdot R_{y,i}};\ d\varphi_{z,R} = \frac{\sum d\varphi_{z,i} \cdot V_i \cdot R_{z,i}}{\sum V_i \cdot R_{z,i}},$$

respectively.

The initially determined rotation vector is defined by $\vec{\mu} = \begin{pmatrix} d\varphi_{x,R} \\ d\varphi_{y,R} \\ d\varphi_{z,R} \end{pmatrix}$ and normalized rotational axis by $\vec{n}$, which is calculated as:

$$\vec{n} = \frac{\vec{\mu}}{|\vec{\mu}|}$$

The angle of rotation $\theta = |\vec{\mu}|$ is defined by the magnitude of the vector and the transformation matrix $\boldsymbol{R}_N$ is calculated as follows:

$$\boldsymbol{R}_N(\vec{n},\theta) = \begin{pmatrix} n_x^2\cdot(1-\cos(\theta))+\cos(\theta) & n_x\cdot n_y\cdot(1-\cos(\theta))-n_z\cdot sin(\theta) & n_x\cdot n_z\cdot(1-\cos(\theta))+n_y\cdot sin(\theta) \\ n_x\cdot n_y\cdot(1-\cos(\theta))+n_z\cdot sin(\theta) & n_y^2\cdot(1-\cos(\theta))+\cos(\theta) & n_y\cdot n_z\cdot(1-\cos(\theta))-n_x\cdot sin(\theta) \\ n_x\cdot n_z\cdot(1-\cos(\theta))-n_y\cdot sin(\theta) & n_y\cdot n_z\cdot(1-\cos(\theta))+n_x\cdot sin(\theta) & n_z^2\cdot(1-\cos(\theta))+\cos(\theta) \end{pmatrix}$$

First tests of the code for simple cases soon revealed that the initial estimates for the rotation vector and angle were not accurate enough for our application, and that an iterative correction of these values is necessary. For the iteration process, the superscript index (j) is introduced, and the initially determined values for the rotation vector and the angle are thus denoted by $\vec{\mu}^{(1)} = \vec{\mu},\ \vec{n}^{(1)} = \vec{n}$ and $\theta^{(1)} = \theta$.

For this first approximation of a rotation vector and angle the element displacement $d\vec{x}_{R,i}^{(1)}$ based on the transformation matrix is calculated:

$$d\vec{x}_{R,i}^{(1)} = \boldsymbol{R}_N(\vec{n}^{(1)}, \theta^{(1)}) \cdot \vec{x}_i - \vec{x}_i$$

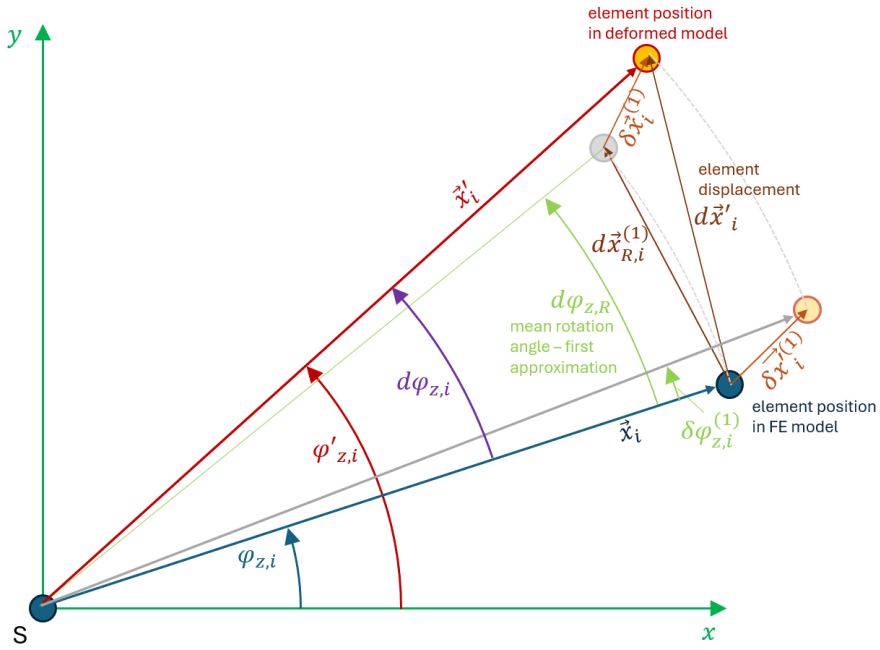

Figure 13. The visualisation of rotation angle calculation around z axis per element

In Figure 13 visualisation of planar rotation angle calculation is represented around z axis. It should be mentioned here that rotation around a single axis of the global coordinate system – like shown here - can be handled easily, but the complexity of the described procedure results from interaction of rotations around all three axes. The element position after rigid body rotation is applied is represented with a grey point. It is a reference position, from which the positional mismatch between the rotational prediction and the actual element displacement from finite element (FE) model $\delta\vec{x}_i^{(1)}$ is measured. This mismatch, transformed to the original element position, is considered as a new element displacement $\delta\vec{x}_i'^{(1)}$ and serves as an input in the iterative loop, which step-by-step minimizes the error:

$$\delta\vec{x}'^{(1)}_i = \boldsymbol{R}_N\left(\vec{n}^{(1)}, -\theta^{(1)}\right)\cdot\delta\vec{x}_i^{(1)}$$

The iterative correction of the rotation vector and rotation angle starts for j=1 to a value, for which the remaining correction of the vector or rotation angle, respectively, is below a given value (e.g. $\left|\theta^{(j+1)} - \theta^{(j)}\right| < 10^{-7}$):

$$\delta\varphi_{x,i}^{(j)} = atan2\left(y_i + \delta y'^{(j)}_i; z_i + \delta z'^{(j)}_i\right) - atan2(y_i; z_i)$$

$$\delta\varphi_{y,i}^{(j)} = atan2\left(x_i + \delta x'^{(j)}_i; -z_i - \delta z'^{(j)}_i\right) - atan2(x_i; -z_i)$$

$$\delta\varphi_{z,i}^{(j)} = atan2\left(x_i + \delta x'^{(j)}_i; y_i + \delta y'^{(j)}_i\right) - atan2(x_i; yz_i)$$

$$\delta\varphi_{x,R}^{(j)} = \frac{\sum \delta\varphi_{x,i}^{(j)} \cdot V_i}{V_{tot}};\ \delta\varphi_{y,R}^{(j)} = \frac{\sum \delta\varphi_{y,i}^{(j)} \cdot V_i}{V_{tot}};\ \delta\varphi_{z,R}^{(j)} = \frac{\sum \delta\varphi_{z,i}^{(j)} \cdot V_i}{V_{tot}}$$

or

$$\delta\varphi_{x,R}^{(j)} = \frac{\sum \delta\varphi_{x,i}^{(j)} \cdot V_i \cdot R_{x,i}}{\sum V_i \cdot R_{x,i}};\ \delta\varphi_{y,R}^{(j)} = \frac{\sum \delta\varphi_{y,i}^{(j)} \cdot V_i \cdot R_{y,i}}{\sum V_i \cdot R_{y,i}};\ \delta\varphi_{z,R}^{(j)} = \frac{\sum \delta\varphi_{z,i}^{(j)} \cdot V_i \cdot R_{z,i}}{\sum V_i \cdot R_{z,i}},$$

respectively.

The corrected rotation vector and rotation angle is:

$$\vec{\mu}^{(j+1)} = \vec{\mu}^{(j)} + \begin{pmatrix} \delta\varphi_{x,R}^{(j)} \\ \delta\varphi_{y,R}^{(j)} \\ \delta\varphi_{z,R}^{(j)} \end{pmatrix};\qquad \vec{n}^{(j+1)} = \frac{\vec{\mu}^{(j+1)}}{|\vec{\mu}^{(j+1)}|};\qquad \theta^{(j+1)} = \left|\vec{\mu}^{(j+1)}\right|$$

Finally, the transformation matrix and the deviation regarding displacements must be updated before the next iteration starts:

$$d\vec{x}_{R,i}^{(j+1)} = \boldsymbol{R}_N\left(\vec{n}^{(j+1)}, \theta^{(j+1)}\right) \cdot \vec{x}_i - \vec{x}_i;\ \delta\vec{x}_i^{(j+1)} = d\vec{x}'_i - d\vec{x}_{R,i}^{(j+1)}$$

The iterative process is illustrated in Figure 14.

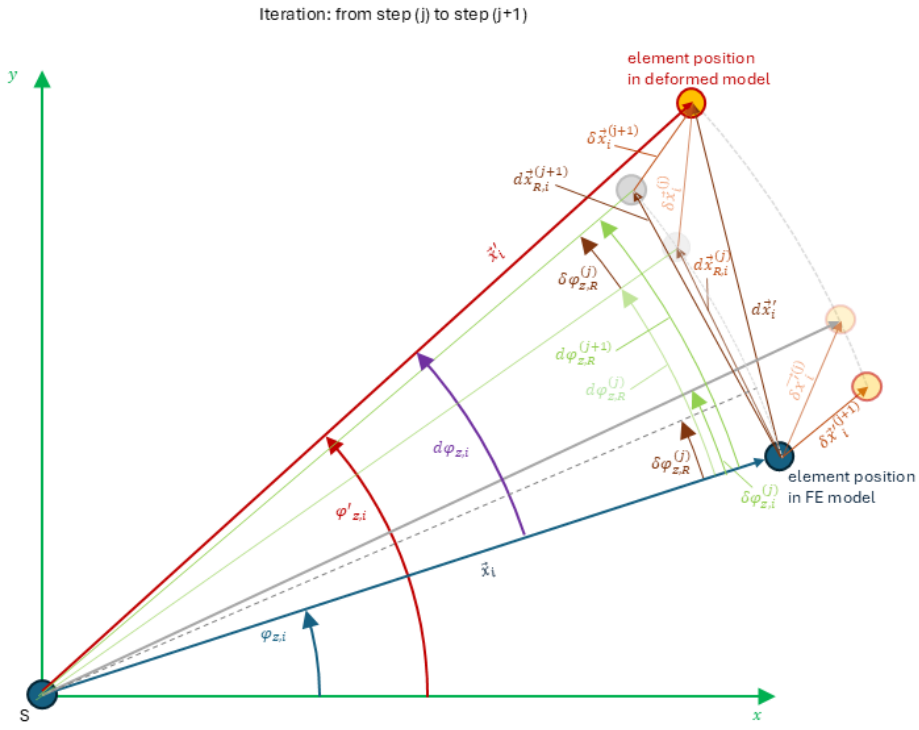

Figure 14. The visualisation of rotation angle calculation around z axis per element from step (j) to step (j+1)

The remaining differences between the actual element displacement and the element displacement caused by an assumed rigid body movement $\delta\vec{x}_i^{(j_{end}+1)} = d\vec{x}_i' - d\vec{x}_{R,i}^{(j_{end}+1)}$ may be due to a homogeneous thermal expansion and deformation of the body itself (due to temperature gradients or mechanical loads). So, in the next step an averaged thermal expansion of the body is determined.

The homogeneous thermal expansion is calculated by comparing the distance of an element from the centre of gravity based on the remaining element displacement $\delta\vec{x}'^{(j_{end}+1)}_i$ with the original distance of the element to the centre of gravity. The corresponding quotient is weighted with the element volume, averaged and used to determine the thermal expansion as follows:

$$\varepsilon_{th} = \frac{\sum \frac{\left|\vec{x}_i + \delta\vec{x}'^{(j_{end}+1)}_i\right|}{|\vec{x}_i|} \cdot V_i}{V_{tot}} - 1$$

In the final part of the APDL script distortion of the body, which refers to asymmetric deformation, is determined by removing:

- Rigid body displacement
- Rigid body rotation
- Isotropic thermal expansion

The total displacement of an element, resulting from the numerical finite-element analysis, can be formulated via:

$$d\vec{x}_i = d\vec{x}_R + R_N\left(\vec{n}^{(j_{end}+1)}, \theta^{(j_{end}+1)}\right) \cdot \left((\varepsilon_{th}+1)\cdot\vec{x}_i\right) + \delta\vec{x}_{dist}$$

Which is transformed into

$$\delta\vec{x}_{dist} = d\vec{x}_i - d\vec{x}_R + R_N\left(\vec{n}^{(j_{end}+1)}, \theta^{(j_{end}+1)}\right) \cdot \left((\varepsilon_{th}+1)\cdot\vec{x}_i\right)$$

to calculate the final distortion of the body due to thermal gradients or mechanical loads.

The above-described evaluation can now be applied to lenses and other optical components to investigate their displacement in the whole system. Assuming that the distortion of these components can be neglected (which of course requires additional assessment), the deformation of the optical system can be directly modified in the CAD software by applying the determined body displacements, rotations and mean volumetric expansions. This allows for implementing clean geometries to the optical software package by STEP files. To verify the APDL script, simplified test cases were set up for a single lens. For the two test cases displacement and rotation values were applied via remote displacements together with an isothermal temperature increment of $\Delta T = 50°C$ (case 1) and a temperature gradient starting from $\Delta T_1 = 40℃$ at the lower bottom edge and $\Delta T_2 = 60℃$ in the top centre (case 2, cf. Figure 15). In the isothermal case (Case 1), no asymmetric deformation is induced. consequently, the residual distortion output by the algorithm should converge to zero, and any non-zero result represents the numerical error during calculations. In the thermal gradient case (Case 2), a spatially non-uniform temperature field introduces body curvature, which the algorithm must correctly resolve and quantify.

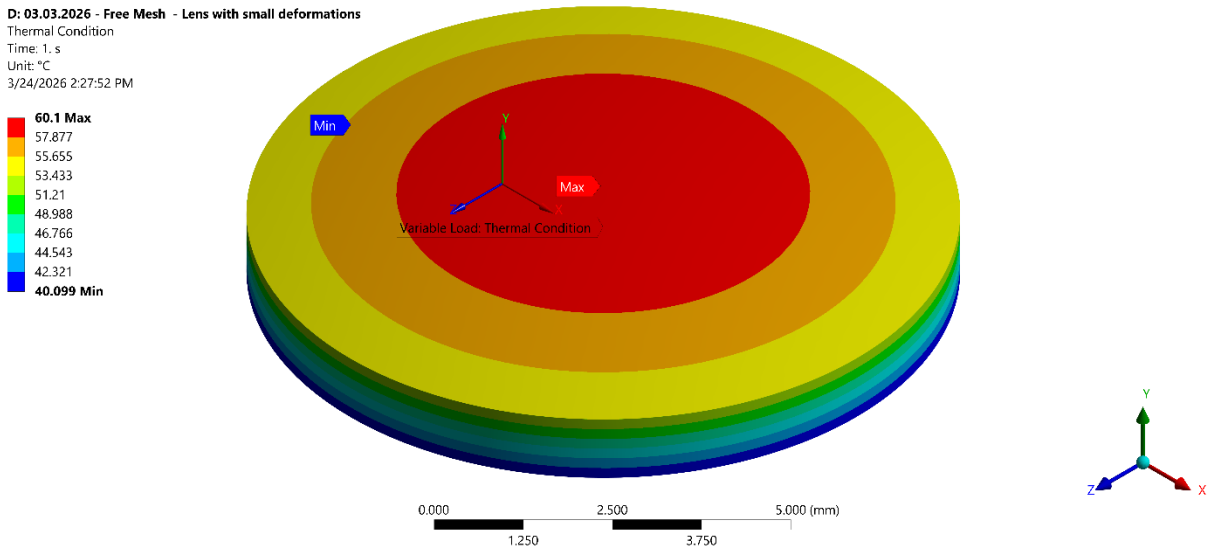

Figure 15. Thermal gradient visualization in the second case scenario

In Table 1 the applied values and results of the evaluation using the APDL script are shown. All displacements and rotational angles were determined within an accuracy of more than 99.65%

Cases	1 (applied)	1 (evaluated)	2 (applied)	2 (evaluated)
$\Delta X\ (mm)$	0.1	0.099996	0.1	0.099996
$\Delta Y\ (mm)$	0.2	0.2	0.2	0.199991
$\Delta Z\ (mm)$	0.3	0.300001	0.3	0.300001
$RX(°)$	0.1	0.1	0.1	0.100354
$RY(°)$	0.2	0.199998	0.2	0.199999
$RZ(°)$	0.3	0.299997	0.3	0.300491
$\Delta T(℃)$	50	-	40-60	-

Table 1: Test case results showing the applied and evaluated values for displacements and rotational angles

For the isothermal load scenario a thermal strain of $\varepsilon_{th} = 0.05011\%$ was determined by the tool, which corresponds to the temperature increment of $\Delta T = 50°C$ and the thermal expansion coefficient of $\alpha_{th} = 10 \cdot 10^{-6} \frac{1}{K}$. The remaining distortion of the lens after applying the predicted body movement as well as the determined thermal expansion is less than $10^{-5} mm$ and this also demonstrates the high accuracy of the tool (cf. Figure 16).

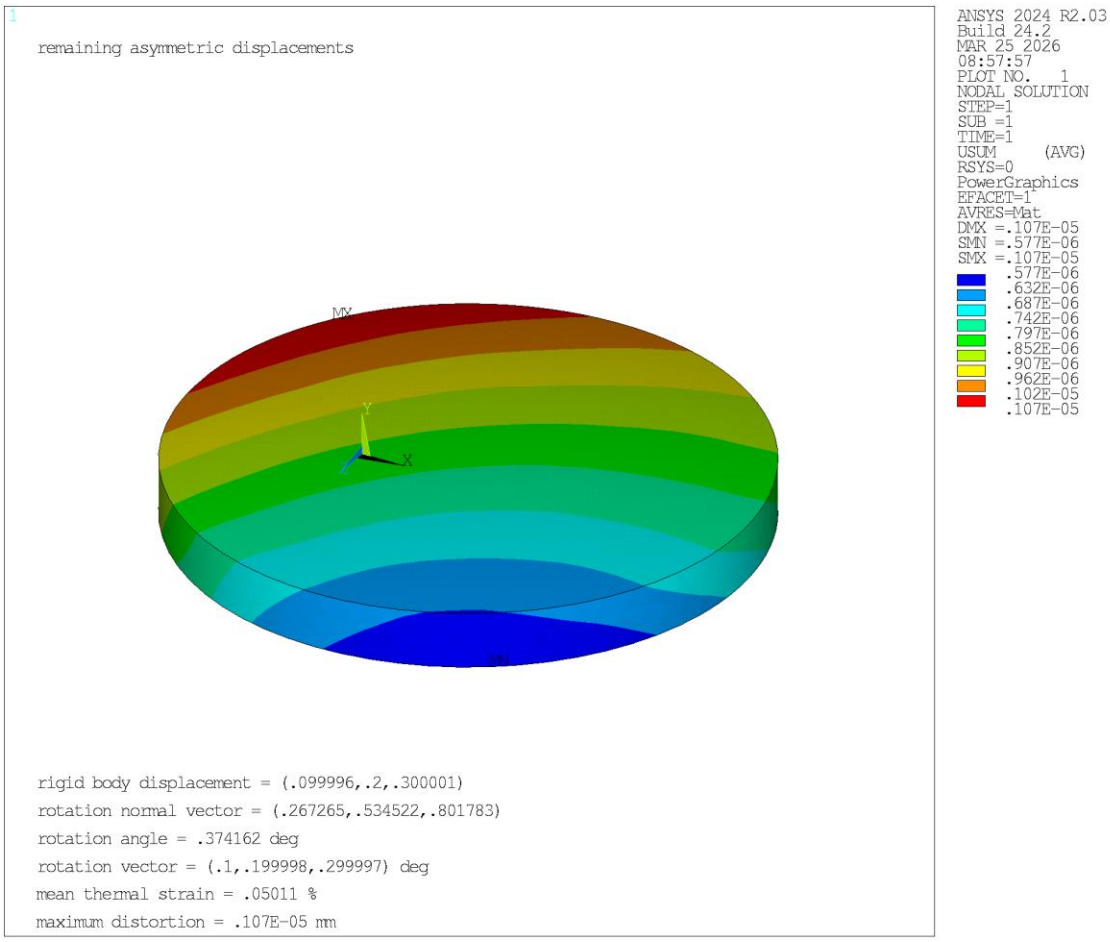

Figure 16. APDL script results of isothermal load scenario

For case 2 the determined average thermal strain is $\varepsilon_{th} = 0.0522\%$ and here the resulting distortion of the lens due to the temperature gradient can clearly be observed (cf. Figure 17).

Up to now there is no further approach to redesign these resulting distortions, shown in Figure 17, as it can be assumed that the lenses in the SHIPAS optical system will not be subjected to significant mechanical stresses or large temperature gradients. However, it is envisaged that fundamental deformations, such as lens deflection, will be derived from the residual deformations and also modelled in the CAD software – for example, by altering the curvature of the lens. This approach would be used to demonstrate later that the residual deformations of the lenses do not, in fact, have a significant influence on the quality of the optical image, and that the previously determined displacements, rotations and thermal expansions determine the quality of the optical image.

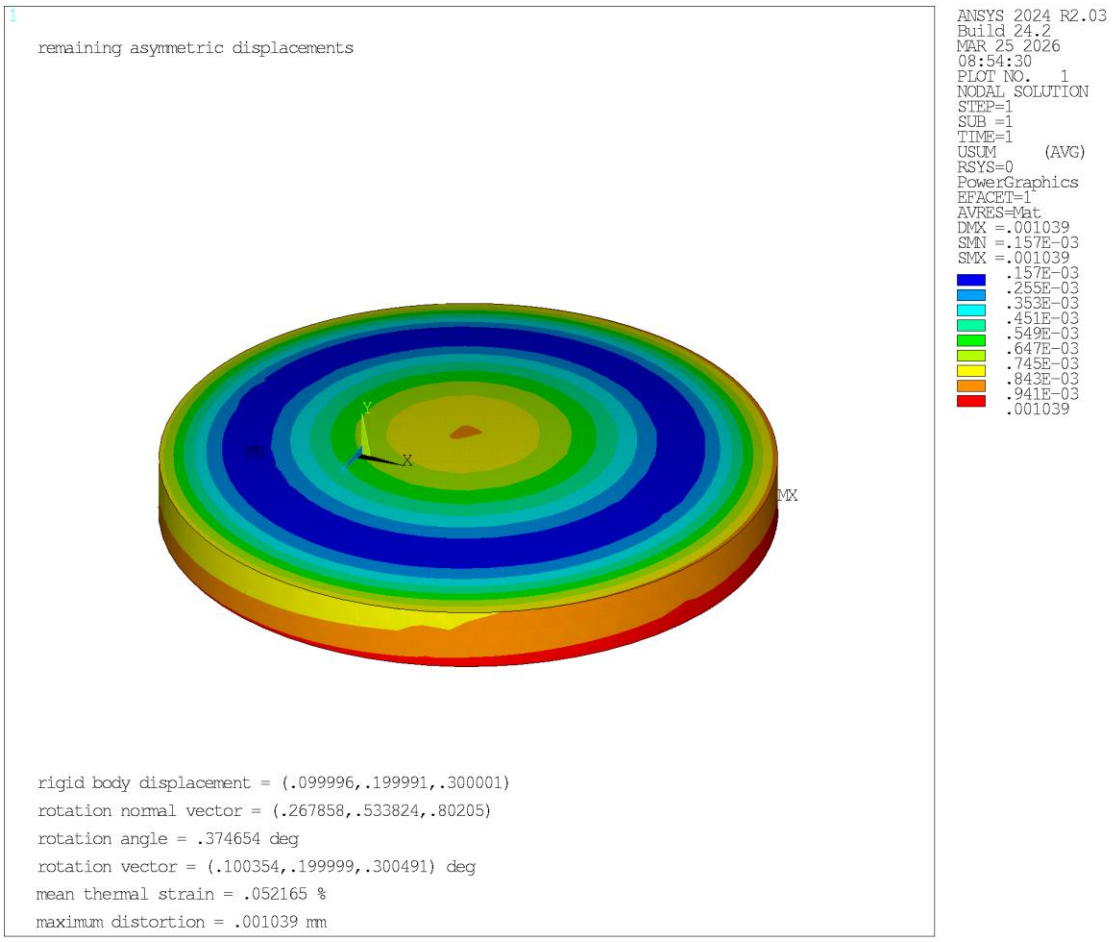

Figure 17. APDL script results of asymmetric thermal load scenario

Based on this verification, it can be assumed, that the APDL script provide precise measurements, capturing rigid body displacement, rotation, thermally induced scaling and asymmetric deformation (thermal strain) of a body.

In a next step the algorithm was used for a real multi body optical system, which is the isolated case of the SHIPAS front optics containing 4 lenses. As a boundary condition the hot case scenario was used for thermo-mechanical coupling, with isothermal temperature starting from $22℃$ to $70℃$ (Figure 18). The thermo-mechanical simulation was performed for the whole system, but in a first step, to just demonstrate the workflow of the STOP analysis, the optical ray tracing was only performed for the front optics.

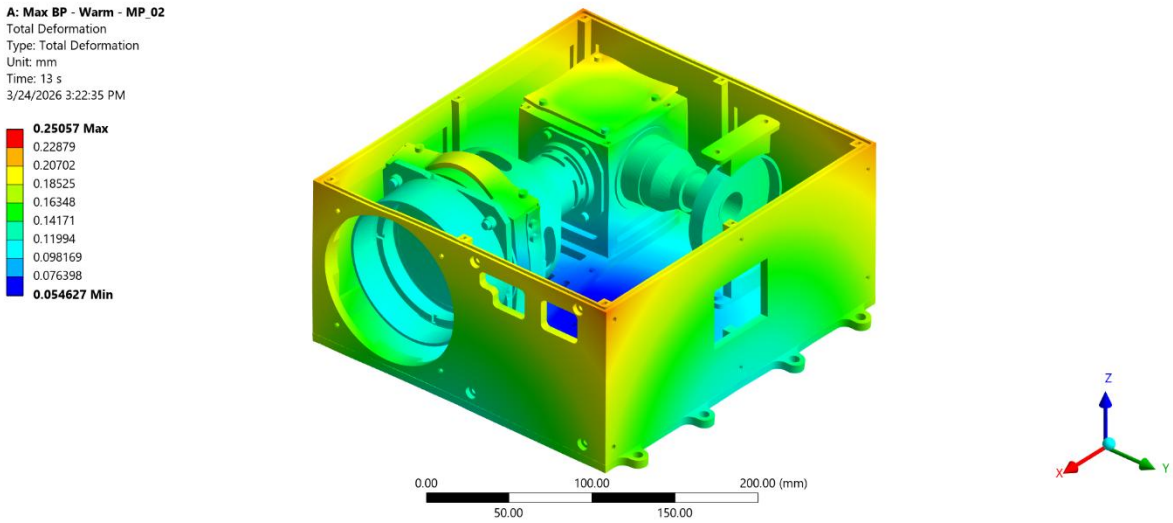

Figure 18. SHIPAS hot case scenario deformation visualization

The APDL script gave following results for each lens (Table 2):

Parameter	Description	Symbol	Lens 1	Lens 2	Lens 3	Lens 4
1	number of Elements	n_{elem}	39842	15433	16358	2097
2	total Volume	V_{tot}	60199.8	15631.1	18171.6	2054.8
3	x displacement of centroid, mm	dx_R	4.92E-02	4.95E-02	4.42E-02	-8.69E-03
4	y displacement of centroid, mm	dy_R	-4.08E-02	-4.15E-02	-4.20E-02	-4.74E-02
5	z displacement of centroid, mm	dz_R	1.11E-01	1.13E-01	1.14E-01	1.16E-01
6	x component of rotation vector	$n_x^{(j+1)}$	-1.91E-01	-1.95E-01	-1.92E-01	-3.11E-01
7	y component of rotation vector	$n_y^{(j+1)}$	9.16E-01	9.19E-01	9.11E-01	6.30E-01
8	z component of rotation vector	$n_z^{(j+1)}$	3.54E-01	3.41E-01	3.64E-01	7.11E-01
9	rotation angle (in degree)	$\theta^{(j+1)}$	6.78E-03	6.58E-03	6.76E-03	6.98E-03
10	thermal strain	ε_{th}	2.77E-04	2.59E-04	1.82E-04	3.41E-04
11	maximum remaining distortion, mm		4.67E-03	5.46E-03	1.98E-03	7.50E-04

Table 2: Evaluated values for displacements, rotational angles, thermal strain and maximum remaining distortion for the front optics system of SHIPAS

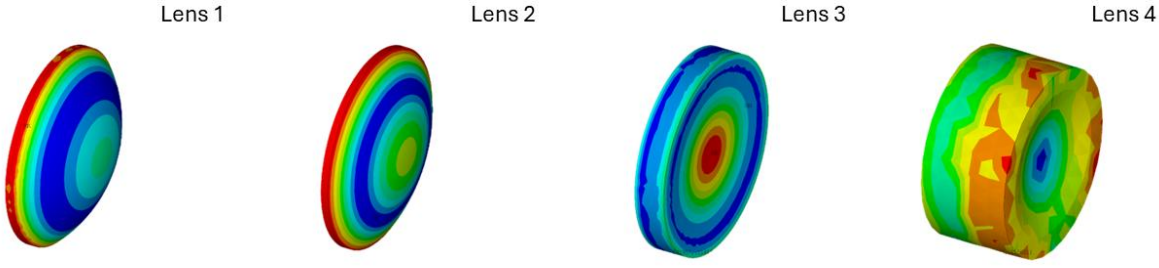

Figure 19. Remaining distortion of front optics lenses

After observing results from Table 2 and Figure 19, it can be assumed that remaining distortion of lenses are mainly caused by the simplified attachment of the lenses to the holders by bonded contact. Moreover, while distortion values are extremely small, they can be neglected for optical simulations.

Based on these results (Table 2), a CAD file for front optics was manually manipulated and the new model of displaced geometry was created (Figure 20).

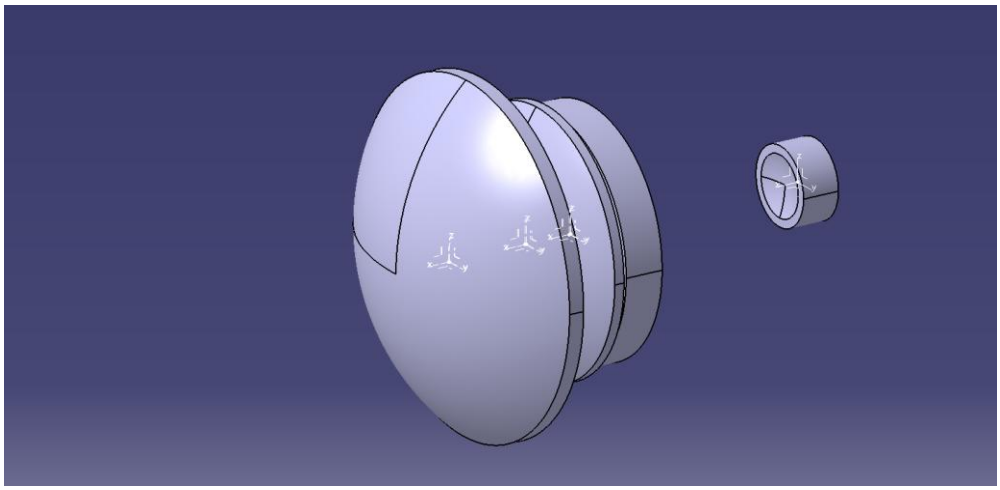

Figure 20. Modified CAD file based on displacement values

This approach enabled to import displaced geometry in Zemax optics studio as a STEP file, therefore, neglecting all the drawbacks of STL file. Afterwards, comparative studies of front optics were made, where ray tracing on ideal and displaced geometries were performed.

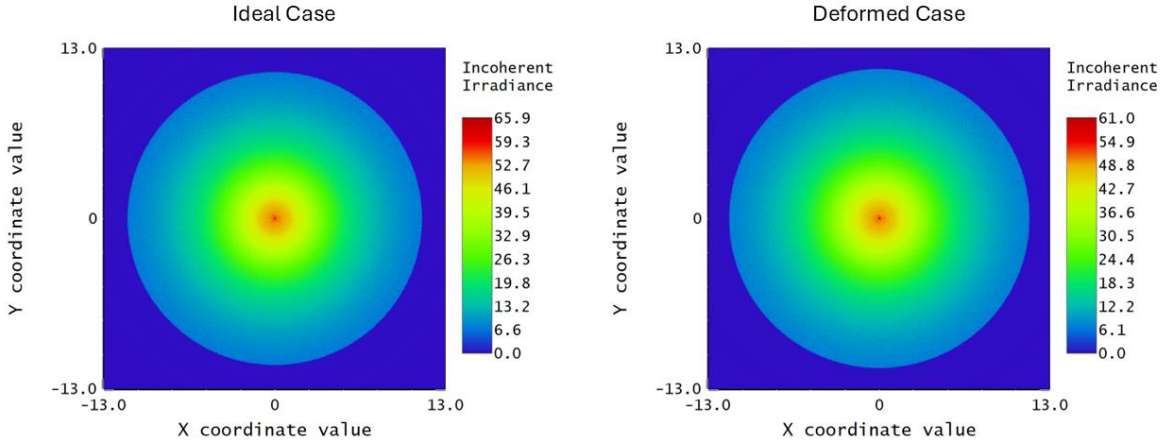

Figure 21. Comparison results between ideal and displaced cases

They key aspect is that proposed data transfer method via APDL script provided optical ray tracing results, that remain comparable nature for both ideal and deformed cases, while any kind of file formatting related distortions were resolved. Thus, it can be concluded that actual numerical differences of peak values in these results are caused by thermally induced deformations, which can be observed in the Figure 21.

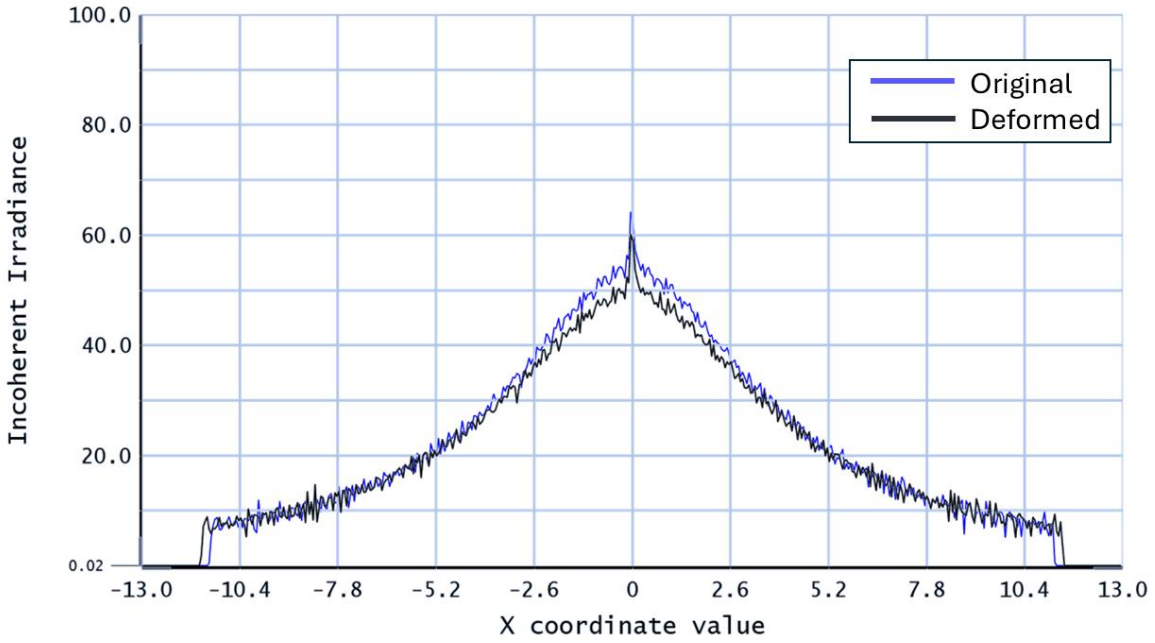

Figure 22. Cross sectional results from comparison

Meanwhile, decrease of whole irradiance field can be observed with a clear comparison visualisation on a cross-sectional result in Figure 22.

8 Conclusion

During these studies the comparative analysis were made in Zemax between 3D files of various formats: STEP, STL and STEP made from smoothed STL file in Space Claim module of Ansys Workbench. The original STEP file was taken as a reference of the ideal case. All other variations provided significant distortion of image. Thus, alternative workflow was developed via APDL script, which excludes any other formatting rather than STEP files. The script monitors all possible thermally induced mechanical distortions, including rigid body displacement, rotation, thermally induced scaling/shrinkage, and thermal strain or asymmetric deformation of a body.

The new workflow gives possibility to analyse geometrical changes of optical elements after thermo-mechanical coupling and perform optical ray tracing simulations afterwards without surface quality related issues caused by file formatting. After the full STOP analysis of optical subsystem, it was observed that implementing APDL script in STOP workflow provides comparative results eventually. As the next step, validation via experimental tests can be defined, that is crucial to verify the assumption based on engineering judgment to neglect asymmetric deformation results from the workflow. Meanwhile, an additional approach would be to find ways to remodel deformed lenses based on obtained data, by changing the curvature of bodies, or implementing additional deflections. However, it is the part of further development.

9 References

Badás, M., Piron, P., Bouwmeester, J., Loicq, J., Kuiper, H., & Gill, E. (2024). Opto-thermo-mechanical phenomena in satellite free-space optical communications: survey and challenges. *Optical Engineering, 63*, 041206–041206.

Bolognese, J., & Irish, S. (2015). Structural-Thermal-Optical-Performance (STOP) Analysis. *Thermal & Fluids Analysis Workshop (TFAWS 2015).*

Haber, A., Draganov, J. E., & Krainak, M. (2022). Subspace identification of low-dimensional Structural-Thermal-Optical-Performance (STOP) models of reflective optics. *Optical Modeling and Performance Predictions XII*, *12215*, pp. 39–54.

Heijmans, J., Holzlöhner, R., & Müller, M. (2018). STOP process and data sharing steps. *Proceedings of SPIE: Modeling, Systems Engineering, and Project Management for Astronomy VIII, Volume 10705*, (pp. 10705-89). Retrieved from https://www.eso.org/sci/libraries/SPIE2018/10705-89_poster.pdf

Koppen, S., van der Kolk, M., Van Kempen, F. C., de Vreugd, J., & Langelaar, M. (2018). Topology optimization of multicomponent optomechanical systems for improved optical performance. *Structural and Multidisciplinary Optimization, 58*, 885–901.

Watt, T., & Stricker, A. (2023, August 22). SHIPAS satellite-based climate sensor approved for in-orbit testing. *SHIPAS satellite-based climate sensor approved for in-orbit testing*. Retrieved from https://www.euramet.org/publications-media-centre/news/news/shipas-satellite-based-climate-sensor-approved-for-in-orbit-testing

Yang, J., Yao, X., Cai, Y., & Bi, G. (2021). Multiphysics modeling, sensitivity analysis, and optical performance optimization for optical laser head in additive manufacturing. *Applied Sciences, 11*, 868.

Zhang, J., Chen, H., Cava, S. L., & Normanshire, C. (2025). STOP Analysis of High-Power Laser Systems – Part 5. *Ansys Optics Knowledge Base*. Retrieved from https://optics.ansys.com/hc/en-us/articles/42661780285203-STOP-Analysis-of-high-power-laser-systems-part-5

Jül-4451 • April 2026
ISSN 0944-2952

Mitglied der Helmholtz-Gemeinschaft